RESEARCH ARTICLE

Peeling off the surface: Pt-decoration of WSe$_2$ nanoflakes results in exceptional photoelectrochemical HER activity

Péter S. Tóth[1] | Gábor Szabó[1] | Gábor Bencsik[1] | Gergely F. Samu[1] |
Krishnan Rajeshwar[2] | Csaba Janáky[1]

[1]Department of Physical Chemistry and
Materials Science, Interdisciplinary
Excellence Center, University of Szeged,
Szeged, Hungary

[2]Department of Chemistry and
Biochemistry, The University of Texas at
Arlington, Arlington, Texas, USA

Correspondence
Péter S. Tóth and Csaba Janáky,
Department of Physical Chemistry and
Materials Science, Interdisciplinary
Excellence Center, University of Szeged,
Rerrich Sq. 1, Szeged, H6720, Hungary.
Email:
toth.peter.sandor@chem.u-szeged.hu;
janaky@chem.u-szeged.hu

Abstract

Photoelectrochemical (PEC) hydrogen evolution reaction (HER) was studied on exfoliated, pristine and Pt-decorated tungsten diselenide (p-WSe$_2$) nanoflake samples, using a previously developed microdroplet PEC microscopy approach. The WSe$_2$ nanoflakes had well-defined thicknesses as measured by atomic force microscopy, and the Pt nanoparticles (NPs) were deposited by a variable number of atomic layer deposition (ALD) cycles. An exceptionally high photocurrent density of 49.6 mA cm^{-2} (under 220 mW cm^{-2} irradiation) and internal-photon-to-electron-conversion efficiency ($\sim$90% at 550 nm) were demonstrated on these Pt-decorated WSe$_2$ (WSe$_2$-Pt) photocathodes. The Pt NP loading and thickness of WSe$_2$ nanoflakes (in the 24–235 nm range) were used to fine-tune their PEC activity for HER. We found similar charge transfer and surface recombination kinetics of pristine and WSe$_2$-Pt specimens (as assessed by intensity-modulated photocurrent spectroscopy), which indicated significant differences in their bulk properties. X-ray and ultraviolet photoelectron spectroscopies were performed to identify defect states and quantify the density of states around the valence band of WSe$_2$. The elevated temperature of the ALD process and the evolving Pt NP phase conspired to passivate the *sub-surface* (i.e., bulk) defects in the WSe$_2$ nanoflakes, resulting in their vastly improved PEC performance.

KEYWORDS
atomic layer deposition, defect migration, density of states, hydrogen evolution, layered semiconductor, photoelectrochemical kinetics

1 | INTRODUCTION

Transition metal dichalcogenides (TMDCs) have been widely featured in photoelectrochemical (PEC) studies since the 1980s, stemming from their high photocurrent density (in the range of several mA cm^{-2}) for the hydrogen evolution reaction (HER).[1–5] These early studies, based largely on single crystals, unraveled the role of defect states (e.g., cracks, terraces, grain boundaries) in layered TMDCs. Paradoxically, while the electrocatalytic (EC) performance improved for the HER in the presence of edge sites and defects, the PEC properties of these layered materials declined with increasing defect concentration.[6,7]

Exfoliation of layered TMDCs to prepare two-dimensional (2-D) materials has garnered much attention in recent years since the advent of graphene.[8] While

exfoliated nanoflakes allow better utilization of the raw materials, this synthetic strategy also leads to an increase in the number of edges and defects, creating surface states within the bandgap, which in turn act as recombination centers for the photogenerated charge carriers in the metal-chalcogenide semiconductor. Thus, increasing the photoelectrode area from micrometer-range to mm^2 or cm^2 size, which is much-needed for solar energy conversion applications, unfortunately has the deleterious consequence of also suppressing the PEC activity to the $\mu A\ cm^{-2}$ range.[9–11]

Charge carrier recombination via defect states was recognized early on, in the use of Pt nanoparticles (NPs) on 2-D material surfaces to improve PEC activity for a targeted application (e.g., HER).[2,12–15] So far, however, the deposited Pt NPs on tungsten disulfide (WS_2) and WSe_2 surfaces were mostly considered in a *catalytic context* for the PEC HER. Thus, even small amounts of Pt NPs on WSe_2 can act as sinks for the photogenerated electrons and reduce the activation energy for the first HER step, namely the formation of an adsorbed hydrogen atom (Volmer reaction).[2] In this vein, the effect of both Pd and Pt NPs electrochemically deposited on WS_2 bulk single crystals was investigated, ultimately delivering ~5.0 $mA\ cm^{-2}$ photocurrent (at +0.2 V vs. standard calomel electrode (SCE) under 0.5 sun illumination) and 7% quantum efficiency for PEC HER.[16]

More recently, in studies of photocathodes consisting of WSe_2 nanoplatelets, the use of aluminum oxide (Al_2O_3) layers grown by atomic layer deposition (ALD),[11] or electrochemically synthetized Pt NPs, increased the photocurrent by two orders of magnitude with a maximum internal quantum yield of approximately 0.6%.[9] Additionally, this research group achieved an HER photocurrent density of 4.0 $mA\ cm^{-2}$ (at 0.0 V vs. reversible hydrogen electrode (RHE) under 1 sun illumination) on photocathodes comprising approximately 11 nm thick WSe_2 nanoflakes with Pt-Cu catalyst.[17] A champion photoelectrode, consisting of mechanically exfoliated bulk WSe_2 crystals with photoelectrochemically deposited Pt-Ru NPs, was reported by another group with >7% solar-to-hydrogen-conversion efficiency under 1 sun illumination.[18] Prior studies have used in situ electrochemical or photocatalytic Pt NP deposition, or alternately, immobilization of pre-synthesized Pt NPs on the metal-chalcogenide surface.[19,20] To the best of our knowledge, there is only one paper reporting Pt NP deposition using ALD on TMDCs, specifically on MoS_2. The optimized MoS_2-Pt with low Pt mass loading (~2.2 wt%) showed a low onset overpotential (31 mV vs. RHE), and small Tafel slope (52 $mV\ dec^{-1}$), in this case, for *EC* HER in the dark.[21]

On the other hand, the role of Pt NPs in ameliorating the defect solid state chemistry of TMDCs is murkier. There are aspects of surface-related processes, such as impurities, atomic vacancies (sulfur, selenium, etc.), that are known to affect the optoelectronic properties and modulate the charge transport characteristics of 2-D materials.[22,23] The first paper on inter-layer vacancy migration appeared in 2014 for multilayer graphene.[24] In the case of TMDCs, both theoretical and experimental evidence have been presented recently to show heat-induced migration of S-,[25] or Se-vacancies[26] in the respective metal chalcogenides. Regarding other semiconductors, a defect migration process was reported for TiO_2, where the number of surface oxygen vacancies increased on Pt-decorated TiO_2 by migration of bulk vacancies to the surface. A vacuum annealing process was used to drive the migration and passivate these incipient defects; the net outcome was an enhancement in the photocatalytic activity.[27] Additionally, in the case of a noble metal-layered material composite, the Ag NPs enhanced the selectivity of secondary hydroxyl oxidation in glycerol and further accelerated the corresponding kinetics.[28]

Herein, we demonstrate record high photocurrent and photon-to-electron conversion efficiency values for Pt-decorated WSe_2 (hereafter WSe_2-Pt) nanoflake photocathodes, where Pt NPs were deposited by ALD. The effect of WSe_2 nanosheet thickness as well as Pt surface loading was carefully quantified, as elaborated below. The relative enhancement of the PEC HER activity was shown to be independent of nanosheet thickness, diagnosing that the Pt NPs acted as *both* passivating agents *and* catalyst sites. Band structure and density of states (DOS) data of heat-treated WSe_2 and WSe_2-Pt samples pointed to a photoactivity enhancement mechanism involving bulk defects (vacancies) in WSe_2 migrating to the surface to be subsequently passivated by the Pt NPs.

2 | METHODS

2.1 | Preparation of WSe_2 and WSe_2-Pt nanoflakes

WSe_2 single crystals (from HQ Graphene) were mechanically exfoliated on insulating oxidized silicon-coated silicon (SiO_2/Si) wafers (from Graphene Supermarket) using the mechanical "Scotch-tape" cleavage method as reported elsewhere.[29] The nanoflakes were then electrically contacted using carbon paste (from Electron Microscopy Sciences) and a copper wire. All PEC and AFM measurements were performed on such mechanically exfoliated nanoflakes. The dispersions of liquid phase-exfoliated (LPE) 2-D crystals (for transmission electron microscopy [TEM] and X-ray/ultraviolet photoelectron spectroscopy [XPS/UPS] studies) were produced ultrasonically and

sorted by area and thickness using centrifugation, to obtain size-selected nanoflakes. Subsequently, the nanosheet-containing dispersions were chosen to deposit films on glassy carbon (from Alfa Aesar) electrodes (for XPS/UPS measurements) using a modified Langmuir–Blodgett method,[29,30] and onto lacey carbon Cu-grids (for TEM characterization; Electron Microscopy Sciences) by the "fishing out" technique from dispersions (see more details regarding the exfoliation techniques in the Supporting Information). Platinum NPs were synthesized by the ALD technique using a high aspect ratio chamber of Beneq TFS200 equipment. Each synthesis was executed with 1 and 1.5 s of Pt and O_2 precursors pulse time, respectively, and 8 s of purge with N_2 gas between the introduction of the precursors. The deposition temperature was 300°C with 1 mbar vacuum in the deposition chamber. Therefore, the WSe_2-Pt-1-cycle, WSe_2-Pt-3-cycle, and WSe_2-Pt-5-cycle samples were prepared using 1, 3, and 5 cycles of Pt deposition, respectively. A shorter deposition was made as well using only 500 ms pulse time of the Pt precursor; the resulting sample was named: WSe_2-Pt-1s-cycle. Additionally, the WSe_2 films on glassy carbon electrodes were heat-treated using the same conditions as for the Pt ALD, but in this case, in the absence of the precursors; these samples were treated at 300°C in a vacuum and named WSe_2-HT.

2.2 | Characterization

The selected nanoflakes were identified by optical microscopy, followed by morphological characterization. Atomic force microscopy (AFM, NT-MDT Solver AFM microscope), operated in the tapping mode with a silicon tip on a silicon nitride lever (Nanosensors, Inc., SSS-NCH-type 15 -μm long silicon needle with 10° half cone angle and 2-nm radius curvature) was used to analyze the nanoflake thickness. The morphology of LPE-prepared WSe_2 nanoflakes and deposited Pt NPs were characterized by capturing TEM images (FEI Tecnai G^2 20 X-Twin type, operating at an acceleration voltage of 200 kV). Analysis of TEM images was performed using ImageJ software, with the diameter of Pt NPs and statistics measured on 150 particles (in the case of WSe_2-Pt-1s-cycle only 100 particles were considered). The number of Pt NPs were counted by TEM images using 100×100 nm squares for 1-, 3-, and 5-cycle depositions.

X-ray photoelectron spectroscopy (using Mg $K\alpha$) was carried out on a SPECS instrument equipped with a PHOI-BOS 150 MCD 9 hemispherical analyzer. The analyzer was used in fixed analyzer transmission mode with 40 eV pass energy for the survey scans and 20 eV pass energy for the high-resolution scans. Charge referencing was done to adventitious carbon (284.8 eV) on the sample surface as a reference. For XPS band deconvolution, CasaXPS commercial software package was used. UPS was performed with a He (I) excitation (21.22 eV) source. An external bias of 10 V was applied to the samples to accelerate secondary electrons to the analyzer. The work function of the samples (φ) was determined by $\varphi = h\nu - (E_{\text{cut-off}} - E_F)$, where $h\nu$ is the photon energy of He(I) (21.22 eV), E_{cutoff} is the secondary electron cutoff energy, and E_F is the Fermi energy; further details are given elsewhere.[31]

The components and details of our custom-developed PEC microscopy approach are given elsewhere (more details can also be found in the Supporting Information).[29] All electrochemical measurements were performed by a PGSTAT302N potentiostat (Metrohm-Autolab). All potentials were measured against the Ag/AgCl reference electrode in 6 M LiCl, approximately +0.19 V on the standard hydrogen electrode (SHE) scale. The linear sweep voltammetry (LSV) traces were collected at 5 mV s^{-1} potential scan rate. The WSe_2 and WSe_2-Pt electrodes were held at −1.5 V constant potential (Ag/AgCl$_{6 \text{ M LiCl}}$) during the incident photon-to-current conversion efficiency (IPCE) measurements. The irradiance was measured before and after each PEC measurement, and it was 226 ± 10 mW cm^{-2} in all cases. This unusual light intensity was a result of our special PEC microscopic setup. Intensity-modulated photocurrent spectroscopy (IMPS) was carried out using the same system, but in this case, the potentiostat was equipped with a FRA32 module and LED driver kit (Metrohm-Autolab). The IMPS data were recorded in the frequency range from 20 kHz to 0.1 Hz, using sinusoidal intensity modulation and bias illumination by a white light LED (irradiance: 35 mW cm^{-2}). The amplitude of the sinusoidal modulation was 10% of the original intensity. A pool of 25 WSe_2 nanoflakes was investigated with different thicknesses, and three individual droplets were deposited on each nanoflake in three different spots. For the IMPS measurements, thickness ranges centering around 50, 150, and 250 nm were used; three replicates were run. The deposited droplets were stable to 4–150 μm in diameter. All measurements were performed at ambient temperature (23–24°C). The quoted errors are standard deviations from replicates.

3 | RESULTS AND DISCUSSION

3.1 | Morphological and structural attributes of WSe_2 and WSe_2-Pt

Figure 1A illustrates our microdroplet-based PEC approach, which was applied to explore the PEC performance of WSe_2 nanosheets.[29] Briefly, the mechanically
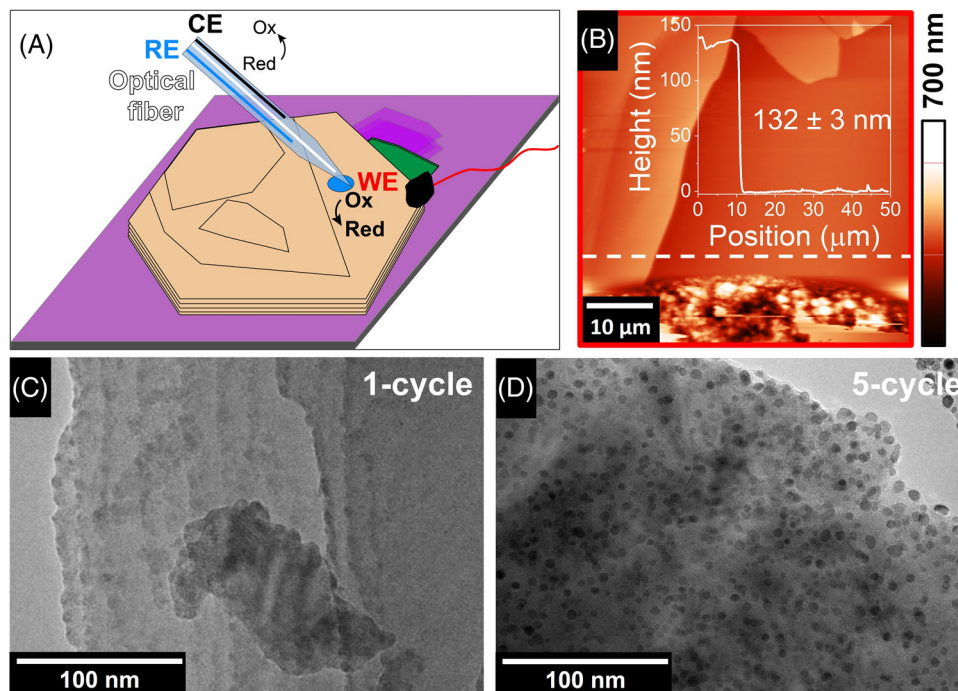
FIGURE 1 Morphological and structural characterization of WSe$_2$ and WSe$_2$-Pt nanoflakes. Scheme of the microdroplet-based photoelectrochemical (PEC) setup (A) atomic force microscopy image of a selected bulk WSe$_2$ nanoflake on oxidized silicon-coated silicon substrate (B). The inset shows the vertical profile of the WSe$_2$ nanoflake from the region highlighted by the dashed white line with a thickness of 132 ± 3 nm. Transmission electron microscopy (TEM) images of WSe$_2$-Pt-1-cycle (C), and WSe$_2$-Pt-5-cycle specimens (D).

exfoliated WSe$_2$ nanoflakes, immobilized on SiO$_2$/Si wafers (hereafter WSe$_2$), were contacted with carbon paste and served as the working electrode, while the area of a microdroplet deposited on the WSe$_2$ specimen defined its active working area. In this three-electrode configuration, the reference and counter electrodes, together with an optical fiber used for illumination, were embedded in the microtip.

The thickness of the exfoliated specimens was determined by AFM. Figure 1B shows a sample WSe$_2$ specimen from a studied pool of 25 nanoflakes, with an average thickness of 132 ± 3 nm. Overall, we studied WSe$_2$ nanoflakes with thicknesses ranging between 24 and 235 nm. ALD protocols were used to deposit Pt NPs on the WSe$_2$ nanoflakes, applying 1, 3, or 5 cycles (with 1 s of Pt precursor pulse time) and one with a shorter cycle (500 ms of Pt precursor pulse time), and these specimens are named hereafter WSe$_2$-Pt-1-cycle, WSe$_2$-Pt-3-cycle, WSe$_2$-Pt-5-cycle, and WSe$_2$-Pt-1s-cycle, respectively. Considering the high catalytic activity of Pt NPs for PEC HER, their loading was kept at max. 5 cycles to exploit the synergistic effect between the constituents.[32]

The morphology of the deposited Pt NPs on the WSe$_2$ surface was investigated by TEM (Figure 1C,D). Interestingly, we found an increase in the number of Pt NPs, while their size remained identical (about 6 ± 1 nm) independently of the number of ALD cycles. The pulse time

of the precursors, the temperature of the chamber, the number of the cycles, the substrate, reagents, and the type of ALD method are all very important factors affecting the size of Pt NPs deposited by ALD. As reported by Wang et al., ALD synthesis using MeCpPt(Me)$_3$ and oxygen precursors at 300°C results approximately 2 nm Pt NPs employing only 1 cycle,[33] while at higher temperatures Pt atoms form larger clusters.[34] Additional TEM images and a histogram of the Pt particle diameters for the WSe$_2$-Pt-1-cycle sample are given in the Supporting Information (Figure S1). The increase of the coverage of Pt NPs on the WSe$_2$ nanoflakes with the number of cycles without any significant change in the particle size can be explained by the ALD mechanism.

During the first step, the WSe$_2$ surface is exposed to the Pt precursor, trimethyl(methylcyclopentadienyl) platinum(IV) (MeCpPtMe$_3$). The precursor ligands react with WSe$_2$ surface-adsorbed oxygen creating a Pt seed, then subsequent oxygen exposure forms a new adsorbed oxygen layer on top of the Pt seeds surface.[35–37] Additionally, the TEM images show that the Pt NPs nucleated initially on the edges and the coverage became subsequently more uniform due to the higher chemical activity of the edge versus the basal plane.[11,38,39] Applying additional ALD cycles, the basal plane of WSe$_2$ samples gradually became more active for binding the Pt precursor as shown later. The similar Pt particle size in the case of different samples helps to
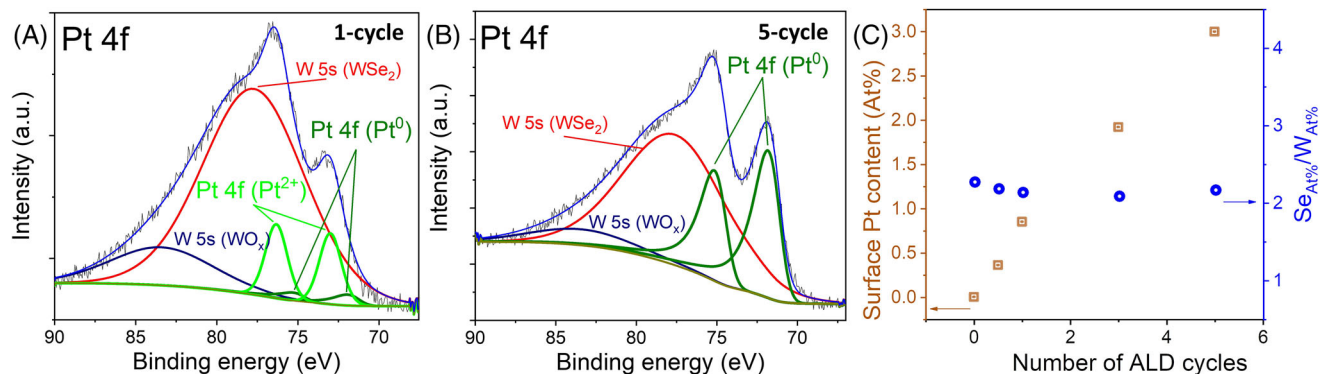
FIGURE 2 High-resolution Pt 4f XPS spectra of WSe_2-Pt-1-cycle (A), and WSe_2-Pt-5-cycle (B) samples, the core levels and oxidation states are labeled in all cases. Pt content of surface (orange square symbols), and Se/W (blue circle symbols) atomic ratio (C) as a function of the number of Pt deposition cycles (extracted from XPS data).

compare their inherent activity by deconvoluting possible size effects.

The surface elemental composition of the WSe_2-Pt samples was investigated by XPS (Figures 2A,B, S2). The survey spectra (Figure S2A) showed O and C content, beyond W and Se, related to surface-adsorbed adventitious carbon, water and oxygen bound to Pt and/or W on the surface.[35,37] The surface Pt content increased with the cycle number, while the $Se_{At\%}/W_{At\%}$ ratio was ~ 2.1 for all specimens showing a Se-rich surface (c.f., Figure 2C). High-resolution Pt 4f XPS spectra were analyzed to probe the oxidation state of Pt on the WSe_2 nanoflakes. In the case of WSe_2-Pt-1s-cycle, WSe_2-Pt-1-cycle, and WSe_2-Pt-3-cycle samples, both Pt^0 and Pt^{2+} signals were observed. The Pt^{2+} likely existed in the form of a surface PtO_x species.[40] The Pt^0 / Pt^{2+} ratio was dependent on the number of Pt deposition cycles (Table S1). The WSe_2-Pt-1s-cycle and WSe_2-Pt-1-cycle samples contained the most Pt^{2+}, while the amount of Pt^0 increased with the ALD cycle number. The presence of Pt^{2+} in the case of lower cycle number WSe_2-Pt specimens can be explained by the oxidative ALD process.[37] At the end of one deposition cycle, the Pt on the WSe_2 surface had an oxygen-rich surface layer, which could then react with the next Pt precursor in a subsequent ALD cycle to deposit more "metallic" (Pt^0) on the same site. At the end of this ALD cycle, the O_2 dose converted more Pt precursor to Pt^0 and also recreated an oxygen-rich surface layer. However, as more Pt^0 was deposited, the relative amount of the metallic Pt^0 to Pt^{2+} also shifted. This behavior, in which the initial stages of ALD deposition favored the formation of PtO_x species, has also been shown for Al_2O_3 substrates.[40] In the case of WSe_2-Pt-5-cycle specimen, the fitting was performed by considering metallic surface Pt species only (Figure 2B) as the contribution of oxidized species was negligible.

3.2 | Effect of Pt loading on the PEC behavior

Our microdroplet-based approach facilitated the PEC activity of the specimens to be monitored in the same location of the selected WSe_2 nanoflakes before and after Pt deposition. Figure 3A depicts a four-fold enhancement in the photocurrent density upon depositing 1-cycle of Pt on a WSe_2 nanoflake with 230 ± 4 nm thickness as a demonstrative example. The irradiance was measured before and after the PEC measurements, which was 217 mW cm^{-2} in this case. To compare the activity of samples with different thickness and Pt loadings, the irradiance was carefully monitored in all the cases (226 ± 10 mW cm^{-2} for all the measurements presented in this study).

The IPCE values recorded for the WSe_2 and WSe_2-Pt-cycle-1 specimens peaked in the 500–550 nm range (Figure 3B). A cutoff value of ~920 nm was determined, giving a 1.34 eV bandgap value, which agrees with literature values.[41] After Pt deposition, the quantum efficiency increased up to 81%–90 % showing that almost every absorbed photon generates an electron-hole pair. More LSV and IPCE curves recorded for WSe_2-Pt-cycle-1 samples with different thicknesses are shown in the Supporting Information (Figure S3). The steeper slope of the photocurrent evolution on the LSV traces (Figure 3A: between 0.0 V and −0.6 V), compared to the pristine samples, indicates a more efficient charge separation and a faster charge transfer at the semiconductor/electrolyte interface.[42,43] As the thickness (and the light absorption) of the WSe_2 remained practically unchanged after the Pt deposition (note the very small loading), the same number of incident photons should generate the same number of photoelectrons. The increased IPCE values, after the deposition of Pt NPs could be the result of either
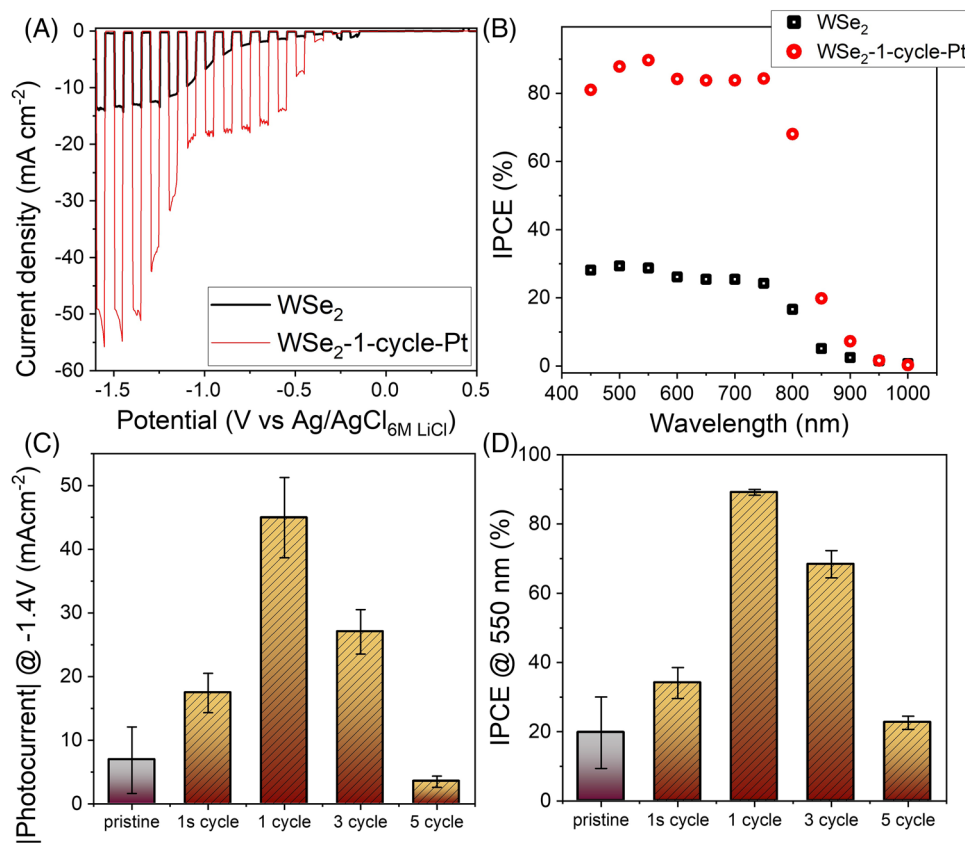
FIGURE 3 PEC activity of WSe$_2$-Pt nanoflakes with a different number of Pt deposition cycles. Selected example linear sweep voltammetries (LSVs) (A), and incident photon-to-current conversion efficiency (IPCE) curves (B) were recorded for the illuminated droplets deposited on WSe$_2$ and WSe$_2$-Pt-cycle-1 nanoflakes in 1 M HCl/6 M LiCl solution. The potential sweep rate for LSVs was 5 mV s^{-1} and the chronoamperometric curves were measured at -1.5 V. The thickness of the WSe$_2$ nanoflake was 230 ± 4 nm. The relative improvement in the photocurrent (C), and quantum efficiency (D) in the function of Pt deposition cycles are shown by bar charts. The thickness of WSe$_2$ nanoflakes for the different loadings was 211 ± 20 nm. The PEC activity of each nanoflake was replicated at three spots. The irradiance was 217 mW cm^{-2} in (A, C).

(catalytic) acceleration of the charge carrier transfer step or the suppression of charge carrier recombination (or both).

The relative growth of current density (Figure 3C) and IPCE (Figure 3D) exhibited a maximum for the WSe$_2$-Pt-1 cycle specimen, indicating the highest PEC activity (in these comparisons the thickness of WSe$_2$ sheets was in the range: 211 ± 20 nm). The decrease in both the photocurrent density (Figure 3C) and the IPCE values (Figure 3D) in the case of WSe$_2$-Pt-cycle-3 and WSe$_2$-Pt-cycle-5 samples suggests a light blocking effect from the increasing amount of Pt NPs (i.e., surface concentration) resulted by the further deposition cycles (Table S1).[44]

The WSe$_2$-Pt-cycle-1 sample showed the highest photocurrent density and IPCE value, simultaneously having the lowest (16%) Pt^0, and highest (84%) Pt^{2+} content on its surface. This implied a relationship between the outstanding PEC activity and the oxidation state of Pt NPs. To monitor the fate of the Pt NPs on the surface of the samples after the PEC reaction, XPS characterization on the same sample was performed at different stages: (i) freshly pre-

pared WSe$_2$ sample, (ii) after 1-cycle Pt deposition by ALD, (iii) after the PEC studies in 1 M HCl and 6 M LiCl (LSV and IPCE traces monitored). The scheme showing these steps and the XPS results are summarized in Figure S4. These measurements revealed that after the PEC measurements: (i) The Se$_{At\%}$/W$_{At\%}$ ratio remained unchanged ($\sim$2), (ii) the composition of the surface Pt was also constant, and (iii) the total Pt content was also similar (i.e., no Pt detachment occurred during the PEC experiments).

3.3 | WSe$_2$ thickness dependence of the PEC activity

The effect of the nanoflakes thickness on the PEC activity was investigated using the 1-cycle ALD Pt sample. Figure 4A shows the absolute photocurrent as the function of the flake thickness, each bar represents one flake with the given thickness, while each black bar has a corresponding red bar as well, as measurements were carried
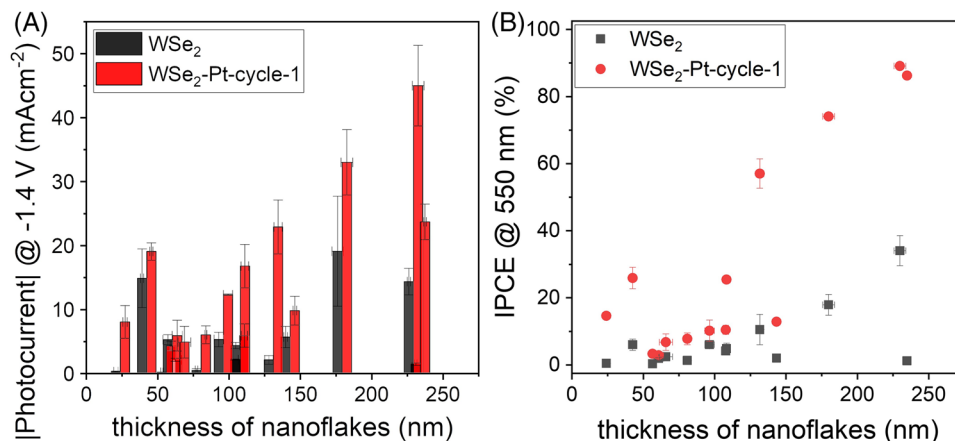
FIGURE 4 Bar chart of the photocurrent (A) and IPCE values (B), recorded for the illuminated droplets deposited on various WSe₂-Pt-cycle-1 samples of different thickness nanoflakes in 1 M HCl/6 M LiCl solution. The irradiance was 217 mW cm^{-2}.

out both before (black bars) and after the Pt deposition (red bars). Horizontal error bars indicate the standard deviation of the flake thickness (from the AFM measurements), while the standard deviation of the photocurrent density comes from 3-3 separate measurements on each flake with the given thickness. The absolute photocurrent enhancement increased with the increasing thickness of the WSe₂ nanoflakes (Figure 4A). This trend could be rationalized by the higher light absorption and the band structure-dependent photogeneration of charge carriers for thicker WSe₂ nanoflakes in comparison with thinner samples.[2,45] A similar pattern was seen in the max. IPCE values, recorded for the photoelectrodes with different thicknesses (Figure 4B). The trends in Figure 4 underline the importance of surface versus bulk processes in the photoactivity of these TMDC samples.

The kinetics of PEC HER on WSe₂ and WSe₂-Pt photocathodes were examined using IMPS measurements on the same WSe₂ nanoflakes before and after Pt deposition (nanoflake thickness: 50 ± 1, 130 ± 5, 230 ± 4 nm). First, a photovoltammogram was recorded in the microdroplet cell (Figures S5A, S6A, and S7A), followed by the IMPS measurement at different applied potentials resulting in the Nyquist plots of the complex photocurrent response (Figures S5b,C, S6B,C, and S7B,C). These plots were used to calculate the PEC charge transfer (k_{tr}) and surface recombination (k_{sr})[43,46–48] rates (Figures S5D, S6D, and S7D). After modification with Pt NP deposition on WSe₂, a similar trend is observed for k_{tr} for the three samples, the value was slightly higher than for pristine WSe₂, while the k_{sr} showed 1–2 orders of magnitude higher values than k_{tr}. This shows that the catalytic activity of the defect states of WSe₂ and Pt NPs-decorated WSe₂ nanoflakes is similar,[44] the current density is not limited by the charge transfer through the electrode/electrolyte interface. Overall, the IMPS data suggest that surface processes alone

cannot account for the superior PEC performance of the Pt-decorated samples; instead, the bulk charge carrier generation and transport have an impact.

3.4 | Surface passivation of vacuum annealed defects

The fact that only minor differences were seen between the charge transfer rates for WSe₂ and WSe₂-Pt-cycle-1 suggests that the improvement in the PEC behavior must be related to changes in the WSe₂ *bulk*. Such bulk alterations have precedence for other semiconductors as mentioned in the introductory paragraph. Thus, vacuum annealing (at 350°C and 0.06 Pa) resulted in the migration of oxygen vacancies from bulk to the surface of TiO₂, increasing the concentration of these vacancies and the content of active Pt species on the surface.[27] Considering the possibility of a similar process in our WSe₂-Pt system, the surface composition of the samples was studied using only thermal annealing steps (300°C, 100 Pa) in the absence of the Pt or O₂ precursors. The duration of these pretreatments was identical to the 1-, 3-, 5-cycle Pt deposition runs; these specimens are named hereafter: WSe₂-HT-1-cycle, WSe₂-HT-3-cycle, WSe₂-HT-5-cycle, respectively. XPS measurements were carried out to evaluate the elemental composition of the surface of the pristine and these HT WSe₂ samples. In the case of pristine samples, four parallel measurements were acquired. The surface-adsorbed species (adventitious carbon, adsorbed H₂O) was omitted from the quantification of the W, Se, and lattice O values (Table S3). High-resolution Se 3d and W 4f spectra (Figure S8) were analyzed to identify the surface defect states. The formation of W(VI) species was observed whose amount increased with the number of heat treatment (HT) cycles (Figure S9A). Its amount was approximately
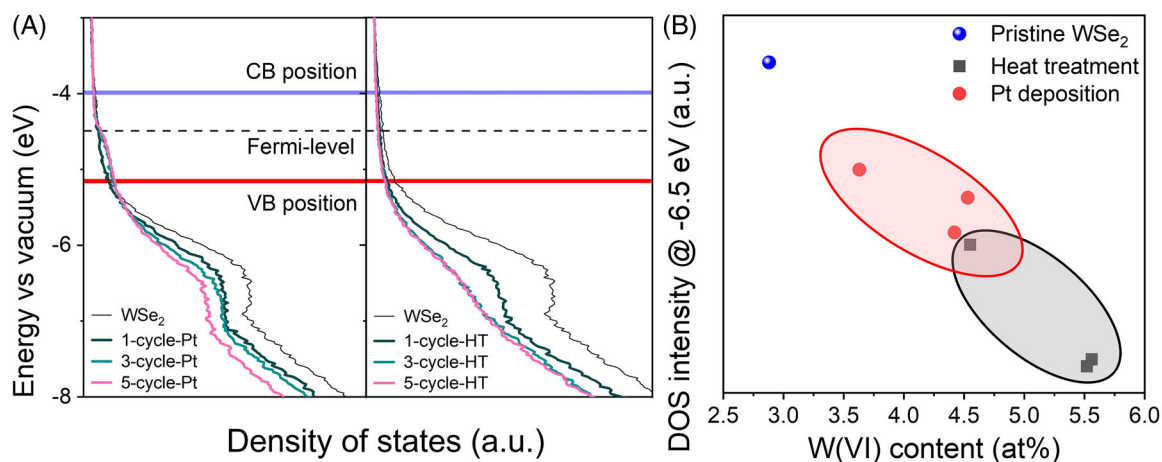
FIGURE 5 (A) Density of states (DOS) plots of WSe_2, heat-treated (cycle-HT), and Pt-deposited (cycle-Pt) samples. (B) The DOS at -6.5 eV of the different samples as a function of W(VI) amount (deduced from XPS).

25%–30% higher for only heat-treated samples, compared to the Pt-decorated specimens. The lattice oxygen content was elevated as well as with the formation of W(VI) in the case of HT samples (Figure S9B); in contrast, a slight decrease in surface selenium was found (Table S3).

To gain further insights into the band structure and DOS of these materials, UPS measurements were carried out (Supporting Information, Figure S10). Based on the VB energy values and Fermi levels, band diagrams were constructed for the WSe_2, WSe_2-Pt, and WSe_2-HT samples (Figure 5A).[41,49,50] The DOS plots showed a maximum peak at −6.5 eV in the VB region (most likely related to filled trap states); whereas the VB edge consisted of W 3d and Se p orbitals. Both HT and Pt NP deposition decreased the population of this energy state. Interestingly, the intensity of the peak at −6.5 eV was lower for the HT samples, compared to the Pt-decorated ones. This DOS loss was equal to the decrease of electron density caused by the formation of W(VI). The change of DOS at −6.5 eV was plotted as a function of the W(VI) amount amplifying the difference between HT and Pt-decorated samples (Figure 5B). At larger amounts of W(VI) in the absence of Pt NPs (HT samples), the electron density and the DOS decreased as the W(IV) transformed to W(VI) losing 2 electrons to the neighboring lattice oxygen. Oppositely, in the case of the Pt-decorated samples, the presence of Pt NPs and their electron density partially compensated for the loss from the incipient W(VI) surface states.

The number of Pt NPs as a function of deposition cycles was extracted from TEM images using 100×100 nm squares (Figure 6A). This number was constant for the nanoflake edges with the increasing deposition cycles, directly proving that the first nucleation spots for Pt NPs were the energetically more favored edge defects. Meanwhile, the number of Pt NPs increased with the cycle number on the basal planes of nanoflakes because the defects in the bulk phase of WSe_2 flakes migrate to the surface (initiated by the vacuum annealing) where they act as nucleation centers for Pt NP deposition. These additional Pt NPs from 3 and 5 cycles could passivate the "freshly" formed W(VI) sites on the surface generated by lattice O migration from the bulk HT caused a decrease in the DOS at −6.5 eV (Figure 5A) due to decreased electron density in the VB. Additionally, we found the lowest DOS and highest W(VI) amount for the WSe_2-HT-cycle-5 sample. Therefore, a sample was prepared with two consecutive steps of ALD protocol: first, a 5-cycle HT (WSe_2-HT-cycle-5), and second, a 1-cycle Pt NPs (Pt-cycle-1) deposition step. Then the PEC behavior of this sample was compared to the PEC performance of previously prepared samples (Figure 6B): (i) only HT (annealing the samples at 300°C, 100 Pa), (ii) Pt deposition (1-cycle-Pt), and (iii) HT followed by subsequent Pt deposition (WSe_2-HT-cycle-5 + Pt-cycle-1). Three different nanoflake thickness regimes were chosen, 53 ± 10, 122 ± 16, and 213 ± 14 nm (Figure 6B).

The PEC activity of the HT samples showed a two-fold increase of the photocurrent compared to the non-HT counterpart (pristine WSe_2), and a similar improvement of photocurrent was seen for the WSe_2-HT-cycle-5 + Pt-cycle-1 specimen. The highest improvement was found for the WSe_2-Pt-cycle-1 specimen where the Pt^{2+} amount was the highest (84%) relative to the 1s-, 3-, and 5-cycle samples (Table S1). The high temperature (300°C in vacuum) during the ALD protocol initiates the migration of defects from the bulk to the surface improving the PEC activity for the only heat-treated sample (WSe_2-HT). The slight improvement of PEC activity is explained by the competition of the surface defects suppression and improvement from the healed bulk phase of WSe_2. While platinum NPs deposition clearly occurred during the high-temperature
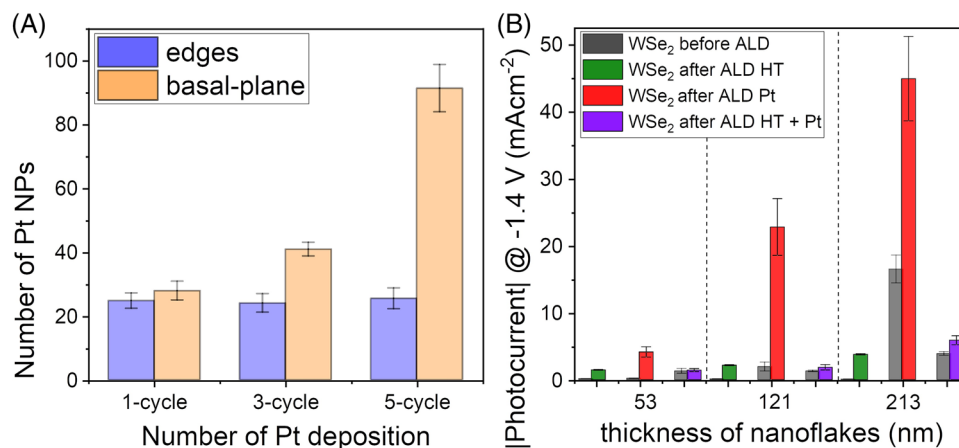
FIGURE 6 Comparison of the PEC activity after atomic layer deposition (ALD) treatments of WSe$_2$ samples. (A) The number of Pt nanoparticles (NPs) as a function of deposition cycles is shown by bar charts. The number of NPs was derived from TEM images from a 100 × 100 nm area. (B) Bar chart of photocurrent evolution before and after ALD treatments as a function of thickness of WSe$_2$ nanoflakes: 53 ± 10, 122 ± 16, 213 ± 14 nm. HT, Pt, and HT + Pt mean heat treatment (HT; 1-cycle), Pt deposition (1-cycle), and HT (5-cycle) coupled with Pt deposition (1-cycle), respectively.

ALD deposition (300°C) because the forming W(VI) surface sites could function as the nucleation centers for the Pt NPs. After Pt deposition, the electron density of these NPs compensates for the reduced electron density in the VB region caused by W(VI) sites.

4 | CONCLUSION

This study focused on an important TMDC, namely, p-WSe$_2$ nanoflakes and ALD deposited Pt NPs for PEC HER. The best-performing 1-cycle Pt WSe$_2$ sample yielded 49.6 mA cm^{-2} photocurrent density at 220 mW cm^{-2} irradiance and about 90% IPCE value (at 550 nm). Evidence was presented for the important role played by bulk defects and their migration to the surface in the overall PEC HER activity. XPS and UPS proved the formation of W(VI) reducing the electron density in the VB region at −6.5 eV. The W(VI) amount increased with the number of HT steps in the ALD chamber, causing only moderate improvement in the photocurrent activity. On the other hand, the electron density from deposited Pt NPs suppressed the DOS decrease caused by W(VI) paving the way for the best PEC performance.

Table 1 shows the PEC performance of our Pt-WSe$_2$ photoelectrode, compared to state-of-the-art materials, to better contextualize the PEC HER activity of the reported photoelectrode. As mentioned in the Introduction section, the early studies from the 1980s on TMDCs for PEC HER were based on *large single crystals* and reported up to 17 mA cm^{-2} photocurrent.[1,2] An important recent work[18] on the PEC HER activity of surface cleaved WSe$_2$ single crystal

with Pt/Ru catalyst, resulted in a high photocurrent (27 mA cm^{-2}, −0.2 V vs. RHE, 100 mW cm^{-2}). Upon concentrated irradiation (200 mW cm^{-2}, similar to our study), 30 mA cm^{-2} photocurrent density was recorded at −0.52 V versus RHE in the presence of 50 mM Ru(NH$_3$)$_6$$^{3+/2+}$. In the case of reports on WSe$_2$ *nanoflakes*, however, the PEC HER performance has been limited to a few mA cm^{-2} photocurrent density.[9,11,17] On the contrary, our study demonstrates that proper defect state passivation (both in the bulk and the surface), together with the ALD-based immobilization of Pt co-catalyst, the PEC performance of nanostructured TDMCs can match that of the respective single crystals, allowing resource-efficient electrode preparation.

In a broader vein, this work highlights (i) The strategies for securing nanostructured TDMC-based photoelectrodes with high PEC activity, (ii) the need to control the migration and passivation of defect states in 2-D materials, and (iii) the importance of properly selecting the parameters of an ALD protocol.

AUTHOR CONTRIBUTIONS
Gábor Szabó prepared the exfoliated WSe$_2$ samples, carried out PEC measurements. Péter S. Tóth performed AFM measurements and analysis. Gábor Bencsik prepared the ALD-coatings on WSe$_2$ samples. Gergely F. Samu carried out the XPS and UPS measurement and analysis. Péter S. Tóth and Csaba Janáky designed the study and supervised the work and also wrote the manuscript with contributions of all authors. Krishnan Rajeshwar and all other authors contributed to the discussion and interpretation of the results. All authors have given approval to the final version of the manuscript.

TABLE 1 Comparison of the photoelectrochemical (PEC) activity, measurement conditions, and preparation methods of WSe_2-based photoelectrodes.

Material	$j_{photo, max}$ (mA cm^{-2})	Conditions	IPCE (%)	Irradiance, lamp (mW cm^{-2})	Electrode type	Refs.
WSe_2	**17** at −0.77 V versus RHE	−1.0 versus SCE, 1 M H_2SO_4	**40** at 600 nm	**100** xenon arc	Single crystal	1
Pt-WSe_2	**11** at 0.0 V versus RHE	0.0 versus RHE, 1 M H_2SO_4	-	**150** solar spectrum	Single crystal	2
Pt/Ru-WSe_2	**27** at −0.2 V versus RHE	−0.2 versus RHE, 0.5 M K_2SO_4, 0.2 M KHP, pH∼4.2	**60** at 550 nm	**100** tungsten halogen	Single crystal	18
	30 at −0.52 V versus RHE	−0.2 versus solution (V), 0.5 M KHP, pH∼2.25, 50 mM $Ru(NH_3)_6^{3+/2+}$	-	**200** tungsten halogen		
Pt/Cu-WSe_2	**4** at −0.1 V versus RHE	−0.1 versus RHE, 1 M H_2SO_4	**37** at 475 nm	**1 sun** Xe arc	Nanoflakes	17
Pt-WSe_2	**0.7** at −0.1 V versus RHE	−0.1 versus RHE, 1 M H_2SO_4	**20** at 550 nm	**1 sun** Xe arc	Nanoflakes	9
Al_2O_3-WSe_2	**2** at 0.14 V versus RHE	−0.4 versus Ag/Ag$^+$, acetonitrile	**13** at 550 nm	**100** LED array	Nanoflakes	11
Pt-WSe_2	**49.6** at −1.2 V versus RHE	−1.4 versus Ag/AgCl, 1 M HCl, 6 M LiCl	**90** at 550 nm	**220** halogen	Nanoflakes	This work
	18 at −0.55 V versus RHE	−0.75 versus Ag/AgCl, 1 M HCl, 6 M LiCl	−			

CONFLICTS OF INTEREST

The authors declare no conflict of interest.

ORCID

Csaba Janáky https://orcid.org/0000-0001-5965-5173

REFERENCES

1. Gobrecht J, Gerischer H, Tributsch H. Electrochemical solar cell based on the d-band semiconductor tungsten-diselenide. *Berichte der Bunsengesellschaft für Phys Chemie*. 1978;82(12):1331-1335. doi: 10.1002/bbpc.19780821212
2. Kautek W, Gobrecht J, Gerischer H. The applicability of semiconducting layered materials for electrochemical solar energy conversion. *Berichte der Bunsengesellschaft für Phys Chemie*. 1980;84(10):1034-1040. doi: 10.1002/bbpc.19800841021
3. Fan F-RF, White HS, Wheeler BL, Bard AJ. Semiconductor electrodes. 31. Photoelectrochemistry and photovoltaic systems with n- and p-type tungsten selenide (WSe_2) in aqueous solution. *J Am Chem Soc*. 1980;102(16):5142-5148. doi: 10.1021/ja00536a002
4. Bicelli LP, Razzini G. Surface behaviour of n-MoSe$_2$ photoanodes in photoelectrochemical solar cells. *Surf Technol*. 1982;16(1):37-47. doi: 10.1016/0376-4583(82)90093-0
5. Abruna HD, Bard AJ. Semiconductor electrodes. 44. photoelectrochemistry at polycrystalline p-type WSe_2 films. *J Electrochem Soc*. 1982;129(3):673-675. http://jes.ecsdl.org/content/129/3/673.abstract
6. Lewerenz HJ, Heller A, DiSalvo FJ. Relationship between surface morphology and solar conversion efficiency of tungsten

diselenide photoanodes. *J Am Chem Soc*. 1980;102(6):1877-1880. doi: 10.1021/ja00526a019

7. Lewerenz HJ, Gerischer H, Lübke M. Photoelectrochemistry of WSe₂ electrodes: comparison of stepped and smooth surfaces. *J Electrochem Soc*. 1984;131(1):100-104. doi: 10.1149/1.2115467

8. Rajeshwar K, Macaluso R. Chalcogenides: solid-state chemistry. *Encycl Inorg Bioinorg Chem*. 2020;:1-23. doi: 10.1002/9781119951438.eibc0038.pub2

9. Yu X, Prévot MS, Guijarro N, Sivula K. Self-assembled 2D WSe₂ thin films for photoelectrochemical hydrogen production. *Nat Commun*. 2015;6(1):7596. doi: 10.1038/ncomms8596

10. Bozheyev F, Harbauer K, Zahn C, Friedrich D, Ellmer K. Highly (001)-textured p-type WSe₂ thin films as efficient large-area photocathodes for solar hydrogen evolution. *Sci Rep*. 2017;7(1):16003. doi: 10.1038/s41598-017-16283-8

11. Yu X, Sivula K. Photogenerated charge harvesting and recombination in photocathodes of solvent-exfoliated WSe₂. *Chem Mater*. 2017;29(16):6863-6875. doi: 10.1021/acs.chemmater.7b02018

12. Velazquez JM, John J, Esposito DV, et al. A scanning probe investigation of the role of surface motifs in the behavior of p-WSe₂ photocathodes. *Energy Environ Sci*. 2016;9(1):164-175. doi: 10.1039/C5EE02530C

13. Zheng J, Lyu Y, Wu B, Wang S. Defect engineering of the protection layer for photoelectrochemical devices. *EnergyChem*. 2020;2(4):100039. doi: 10.1016/j.enchem.2020.100039

14. Lu Q, Yu Y, Ma Q, Chen B, Zhang H. 2D transition-metal-dichalcogenide-nanosheet-based composites for photocatalytic and electrocatalytic hydrogen evolution reactions. *Adv Mater*. 2016;28(10):1917-1933. doi: 10.1002/adma.201503270

15. Zhang J, Wu J, Guo H, et al. Unveiling active sites for the hydrogen evolution reaction on monolayer MoS₂. *Adv Mater*. 2017;29(42):1701955. doi: 10.1002/adma.201701955

16. Baglio JA, Calabrese GS, Harrison DJ, et al. Electrochemical characterization of p-type semiconducting tungsten disulfide photocathodes: efficient photoreduction processes at semiconductor/liquid electrolyte interfaces. *J Am Chem Soc*. 1983;105(8):2246-2256. doi: 10.1021/ja00346a024

17. Yu X, Guijarro N, Johnson M, Sivula K. Defect mitigation of solution-processed 2D WSe₂ nanoflakes for solar-to-hydrogen conversion. *Nano Lett*. 2018;18(1):215-222. doi: 10.1021/acs.nanolett.7b03948

18. McKone JR, Pieterick AP, Gray HB, Lewis NS. Hydrogen evolution from Pt/Ru-coated p-type WSe2 photocathodes. *J Am Chem Soc*. 2013;135(1):223-231. doi: 10.1021/ja308581g

19. Klein A, Pettenkofer C, Jaegermann W, et al. Interface reaction of Pt on p-WSe₂(0001) surfaces. *Surf Sci*. 1992;264(1-2):L193-L199. doi: 10.1016/0039-6028(92)90153-W

20. Ma Z, Konze P, Küpers M, et al. Elucidation of the active sites for monodisperse FePt and Pt nanocrystal catalysts for p-WSe₂ photocathodes. *J Phys Chem C*. 2020;124(22):11877-11885. doi: 10.1021/acs.jpcc.0c01288

21. Ren W, Zhang H, Cheng C. Ultrafine Pt nanoparticles decorated MoS₂ nanosheets with significantly improved hydrogen evolution activity. *Electrochim Acta*. 2017;241:316-322. doi: 10.1016/j.electacta.2017.04.145

22. Gali SM, Pershin A, Lherbier A, Charlier J-C, Beljonne D. Electronic and transport properties in defective MoS₂: impact of

sulfur vacancies. *J Phys Chem C*. 2020;124(28):15076-15084. doi: 10.1021/acs.jpcc.0c04203

23. Lin J, Zuluaga S, Yu P, Liu Z, Pantelides ST, Suenaga K. Novel Pd2Se3 Two-dimensional phase driven by interlayer fusion in layered PdSe₂. *Phys Rev Lett*. 2017;119(1):16101. doi: 10.1103/PhysRevLett.119.016101

24. Liu L, Gao J, Zhang X, Yan T, Ding F. Vacancy inter-layer migration in multi-layered graphene. *Nanoscale*. 2014;6(11):5729-5734. doi: 10.1039/C4NR00488D

25. Inani H, Shin DH, Madsen J, et al. Step-by-step atomic insights into structural reordering from 2D to 3D MoS₂. *Adv Funct Mater*. 2021;31(13):2008395. doi: 10.1002/adfm.202008395

26. Zhang S, Li ML, Jiang M, Xiao H, Scanlon DO, Zu X. Formation and migration of vacancy defects in GeSe and SnSe. *J Phys B At Mol Opt Phys*. 2021;54(3):035003. doi: 10.1088/1361-6455/abd9fd

27. Qiu H, Ma X, Sun C, Zhao B, Chen F. Surface oxygen vacancies enriched Pt/TiO₂ synthesized with a defect migration strategy for superior photocatalytic activity. *Appl Surf Sci*. 2020;506:145021. doi: 10.1016/j.apsusc.2019.145021

28. Liu Y, Wang M, Zhang B, Yan D, Xiang X. Mediating the oxidizing capability of surface-bound hydroxyl radicals produced by photoelectrochemical water oxidation to convert glycerol into dihydroxyacetone. *ACS Catal*. 2022;12(12):6946-6957. doi: 10.1021/acscatal.2c01319

29. Tóth PS, Szabó G, Janáky C. Structural features dictate the photoelectrochemical activities of two-dimensional MoSe₂ and WSe₂ nanostructures. *J Phys Chem C*. 2021;125(14):7701-7710. doi: 10.1021/acs.jpcc.1c01265

30. Cunningham G, Khan U, Backes C, et al. Photoconductivity of solution-processed MoS₂ films. *J Mater Chem C*. 2013;1(41):6899-6904. doi: 10.1039/C3TC31402B

31. Balog Á, Samu GF, Pető S, Janáky C. The mystery of black TiO₂: insights from combined surface science and in situ electrochemical methods. *ACS Mater Au*. 2021;1(2):157-168. doi: 10.1021/acsmaterialsau.1c00020

32. Yoo J, Zazpe R, Cha G, et al. Uniform ALD deposition of Pt nanoparticles within 1D anodic TiO₂ nanotubes for photocatalytic H2 generation. *Electrochem Commun*. 2018;86:6-11. doi: 10.1016/j.elecom.2017.10.017

33. Wang C, Hu L, Lin Y, Poeppelmeier K, Stair P, Marks L. Controllable ALD synthesis of platinum nanoparticles by tuning different synthesis parameters. *J Phys D Appl Phys*. 2017;50(41):415301. doi: 10.1088/1361-6463/aa8709

34. Zhou Y, Muhich CL, Neltner BT, Weimer AW, Musgrave CB. Growth of Pt particles on the anatase TiO₂ (101) surface. *J Phys Chem C*. 2012;116(22):12114-12123. doi: 10.1021/jp302273m

35. Knoops HCM, Mackus AJM, Donders ME, van de Sanden MCM, Notten PHL, Kessels WMM. Remote plasma ALD of platinum and platinum oxide films. *Electrochem Solid-State Lett*. 2009;12(7):G34. doi: 10.1149/1.3125876

36. Aaltonen T, Ritala M, Sajavaara T, Keinonen J, Leskelä M. Atomic layer deposition of platinum thin films. *Chem Mater*. 2003;15(9):1924-1928. doi: 10.1021/cm021333t

37. Sun S, Zhang G, Gauquelin N, et al. Single-atom catalysis using Pt/graphene achieved through atomic layer deposition. *Sci Rep*. 2013;3(1):1775. doi: 10.1038/srep01775

38. Pető J, Ollár T, Vancsó P, et al. Spontaneous doping of the basal plane of MoS₂ single layers through oxygen substitution

under ambient conditions. *Nat Chem*. 2018;10(12):1246-1251. doi: 10.1038/s41557-018-0136-2

39. McDonnell S, Brennan B, Azcatl A, et al. HfO2 on MoS$_2$ by atomic layer deposition: adsorption mechanisms and thickness scalability. *ACS Nano*. 2013;7(11):10354-10361. doi: 10.1021/nn404775u

40. Baker L, Cavanagh AS, Seghete D, et al. Nucleation and growth of Pt atomic layer deposition on Al$_2$O$_3$ substrates using (methylcyclopentadienyl)-trimethyl platinum and O$_2$ plasma. *J Appl Phys*. 2011;109(8):84333. doi: 10.1063/1.3555091

41. Velický M, Toth PS. From two-dimensional materials to their heterostructures: an electrochemist's perspective. *Appl Mater Today*. 2017;8:68-103. doi: 10.1016/j.apmt.2017.05.003

42. Iandolo B, Wickman B, Zorić I, Hellman A. The rise of hematite: origin and strategies to reduce the high onset potential for the oxygen evolution reaction. *J Mater Chem A*. 2015;3(33):16896-16912. doi: 10.1039/C5TA03362D

43. Boudoire F, Liu Y, Le Formal F, Guijarro N, Lhermitte CR, Sivula K. Spray synthesis of CuFeO$_2$ photocathodes and in-operando assessment of charge carrier recombination. *J Phys Chem C*. 2021;125(20):10883-10890. doi: 10.1021/acs.jpcc.1c02282

44. Chen Z, Forman AJ, Jaramillo TF. Bridging the gap between bulk and nanostructured photoelectrodes: the impact of surface states on the electrocatalytic and photoelectrochemical properties of MoS$_2$. *J Phys Chem C*. 2013;117(19):9713-9722. doi: 10.1021/jp311375k

45. Son Y, Wang QH, Paulson JA, et al. Layer number dependence of MoS$_2$ photoconductivity using photocurrent spectral atomic force microscopic imaging. *ACS Nano*. 2015;9(3):2843-2855. doi: 10.1021/nn506924j

46. Ponomarev EA, Peter LM. A comparison of intensity modulated photocurrent spectroscopy and photoelectrochemical impedance spectroscopy in a study of photoelectrochemical hydrogen evolution at p-InP. *J Electroanal Chem*. 1995;397(1-2):45-52. doi: 10.1016/0022-0728(95)04148-9

47. Cass MJ, Duffy NW, Peter LM, Pennock SR, Ushiroda S, Walker AB. Microwave reflectance studies of photoelectrochemical kinetics at semiconductor electrodes. 2. hydrogen evolution at p-Si in ammonium fluoride solution. *J Phys Chem B*. 2003;107(24):5864-5870. doi: 10.1021/jp0300896

48. Zachäus C, Abdi FF, Peter LM, van de Krol R. Photocurrent of BiVO$_4$ is limited by surface recombination, not surface catalysis. *Chem Sci*. 2017;8(5):3712-3719. doi: 10.1039/C7SC00363C

49. Kang J, Tongay S, Zhou J, Li J, Wu J. Band offsets and heterostructures of two-dimensional semiconductors. *Appl Phys Lett*. 2013;102(1):12111. doi: 10.1063/1.4774090

50. Wilson NR, Nguyen PV, Seyler K, et al. Determination of band offsets, hybridization, and exciton binding in 2D semiconductor heterostructures. *Sci Adv*. 2021;3(2):e1601832. doi: 10.1126/sciadv.1601832

SUPPORTING INFORMATION

Additional supporting information can be found online in the Supporting Information section at the end of this article.